buildings

MDPI

Article

Mechanical Properties and Mesoscopic Numerical Simulation of Local Weakening in High-Performance Concrete after 10 Years of Alkali Solution Immersion

Juan Guo [1,2], Jianbo Guo [1,*], Hongfa Yu [1,*], Haiyan Ma [1], Jinhua Zhang [1], Jun Yan [3], Fang Wang [1,2] and Lifang Zhang [1]

[1] College of Civil Aviation, Nanjing University of Aeronautics and Astronautics, No. 29, Yudao Street, Nanjing 210016, China; guojuan@nuaa.edu.cn (J.G.); mahaiyan@nuaa.edu.cn (H.M.); zjh982038@nuaa.edu.cn (J.Z.); wangfang85@nuaa.edu.cn (F.W.); zlf.zj@nuaa.edu.cn (L.Z.)
[2] Xinjiang Vocational and Technical College of Transportation, No. 478, Yongshun Street, Urumqi 831401, China
[3] School of Civil Engineering, Wuhan University, Wuhan 430072, China; jun.yan@whu.edu.cn
* Correspondence: guojianbo@nuaa.edu.cn (J.G.); yuhongfa@nuaa.edu.cn (H.Y.)

Abstract: The natural environment in the high-altitude regions of Northwest China is extremely harsh, characterized by numerous salt lakes. The high concentrations of chloride salts, sulfates, and alkali metal ions in these areas can induce alkali–silica reactions (ASRs) in concrete. These reactions generate harmful gel within the concrete, causing expansion and cracking, which significantly impacts the durability of concrete structures. This study investigates the evolution of the mechanical properties in high-performance concrete (HPC) under long-term ASR by incorporating different admixtures and varying the equivalent alkali content. A three-dimensional random aggregate mesoscopic model was used to simulate static compression tests under various operational conditions. Non-destructive testing methods were utilized to determine the expansion rate, internal, and surface damage variables of the concrete. The experimental results indicate that the 10-year expansion rate differs from the 1-year rate by approximately 1%, and under long-term ASR mitigation measures, the internal damage in the HPC is minimal, though the surface damage is more severe. As the equivalent alkali content increases, the compressive strength of the concrete cubes decreases, initially rising before falling by 5–15% over time. The HPC with only air-entraining agent added exhibited better mechanical performance than the HPC with both air-entraining and corrosion inhibitors added, with the poorest performance observed in the HPC with only a corrosion inhibitor. A relationship was established between the surface and internal damage variables, with the surface damage initially increasing rapidly before stabilizing as the internal damage rose. Numerical simulations effectively describe the damage behavior of HPC under static uniaxial compression. Comparisons with actual failure morphologies revealed that, in the cube compression tests, crack propagation directly penetrated both coarse and fine aggregates rather than circumventing them. The simulations closely matched the experimental outcomes, demonstrating their accuracy in modeling experiments. This study discusses the compressive mechanical properties of concrete under prolonged ASR through a combination of experimental and simulation approaches. It also delves into the impact of surface damage on the overall mechanical performance and failure modes of concrete. The findings provide experimental and simulation support for the concrete structures in regions with high alkali contents.

Keywords: high-performance concrete; salt lake brine; cubic uniaxial compression; mesoscopic model

check for updates

Citation: Guo, J.; Guo, J.; Yu, H.; Ma, H.; Zhang, J.; Yan, J.; Wang, F.; Zhang, L. Mechanical Properties and Mesoscopic Numerical Simulation of Local Weakening in High-Performance Concrete after 10 Years of Alkali Solution Immersion. *Buildings* **2024**, *14*, 1965. https://doi.org/10.3390/buildings14071965

Academic Editor: Francesco Ascione

Received: 13 May 2024
Revised: 16 June 2024
Accepted: 25 June 2024
Published: 28 June 2024

Copyright: © 2024 by the authors. Licensee MDPI, Basel, Switzerland. This article is an open access article distributed under the terms and conditions of the Creative Commons Attribution (CC BY) license (https://creativecommons.org/licenses/by/4.0/).

1. Introduction

Over the past half-century, the alkali–aggregate reaction (AAR) has caused significant damage in many countries, as evidenced by research findings in studies such as those conducted by Peng et al. [1], Rasheed et al. [2], and Yang et al. [3]. Microstructural analyses of concrete reveal that aggregates like sand and stone, which serve as the structural backbone,

often contain reactive mineral components like opal, chalcedony, and cryptocrystalline quartz, which are rich in silica. These minerals can easily undergo alkali–silica reactions (ASR) with the alkalis (Na_2O, K_2O) in cement to form alkali–silica gels. These gels expand upon absorbing water, leading to concrete deterioration, as discussed by Dai et al. [4]. Additionally, temperature is a significant factor influencing the timing and rate of ASR reactions, highlighted in studies by Marko et al. [5]. Since the first report by McCoy and Caldwell [6] in 1951 on the inhibitory effects of small amounts of chemical additives on ASR, extensive research and data accumulation have taken place in countries severely affected by ASR, such as the UK, USA, Canada, and Japan. Compared to incorporating mixed materials, this approach does not require altering construction conditions and can even enhance other properties of engineering concrete, making it more acceptable in contemporary engineering practices, as noted by Dai et al. [7] in another study. Shayan and Ivanusec [8] explored the impact of adding NaOH on the mechanical properties of mortar with both reactive and non-reactive aggregates. Their findings indicated that adding NaOH led to a decrease in the strength of the mortar, and the trend in the strength reduction of mortars containing reactive aggregates was found to be similar to that of mortars without reactive aggregates. Their research also revealed that NaOH interacts chemically with cement, affecting the performance of the resultant solid phases. Hence, high alkalinity is detrimental to concrete strength [9], whether through alkali–aggregate reactions or by influencing cement hydration and the properties of the hydration products.

The research conducted by Cavalcanti [10] has demonstrated that the strength and durability of concrete are significantly compromised over the long term due to the detrimental effects of ASR-induced cracking. Sanchez's findings [11] suggest that under the influence of ASR, concrete exhibits a greater reduction in tensile strength and elastic modulus compared to its compressive strength. Nixon et al. [12] found that a significant decline in the compressive strength of concrete only occurs at high expansion levels, with a 30% reduction in strength at an expansion rate of 5%, while the reduction in tensile strength ranges between 12% and 70% at low expansion levels (0.05%) and 50% and 70% at higher expansion levels (0.2~0.3%). A study by Giaccio et al. [13] investigated the impact of ASR on the mechanical properties of both plain and reinforced concrete, indicating a profound effect on the concrete's tensile strength and elastic modulus. In some cases, ASR did not affect the compressive strength but significantly reduced the Poisson's ratio. Furthermore, extensive research by Dai et al. [14,15] on alkali-activated slag cements has elucidated the fundamental differences in rheological behavior and structural build-up between sodium hydroxide-activated slag pastes and sodium silicate-activated slag pastes.

Incorporating substantial amounts of mineral admixtures like fly ash, silica fume, and slag into high-performance concrete (HPC) has been shown to effectively mitigate the effects of alkali–silica reactions (ASRs) according to research by Feng et al. [16]. A study by Marzouk and Langdon [17] explored the impact of alkali-reactive aggregates on the mechanical properties of both HPC and ordinary Portland concrete (OPC). After curing for 28 days, concrete specimens were immersed in an 80 °C NaOH solution or pure water for a duration of 12 weeks. The findings revealed that OPC with highly alkali-reactive aggregates suffered significant strength losses when soaked in NaOH solution, whereas HPC exhibited minimal strength losses, regardless of whether the aggregates had high or moderate alkali reactivity. Furthermore, research by Fares and Khan [18] investigated the inhibitory effects of HPC composites on ASR. The results indicated that the use of either fly ash (FA) at 45% or silica fume (SF) at 15% alone did not inhibit ASR as effectively as a combined addition of FA and SF (10% FA and 10% SF).

As computer technology has rapidly advanced, researchers have begun to employ numerical simulation techniques supported by high-performance computers to study the unobservable damage phenomena and mechanisms that occur within concrete [19]. Concrete is a heterogeneous multiphase composite consisting of coarse and fine aggregates, cement, and water, and it is often modeled as a three-phase composite material, including aggregates, the interfacial transition zone (ITZ), and mortar. Numerous scholars have

incrementally shifted their research focus from homogeneous models to more diverse mesoscopic models [20–23], thereby upgrading and improving these models to capture a broader spectrum of material complexities.

Researchers have conducted extensive studies on the shape and spatial structure of aggregates within these models. Their investigations have included two-dimensional circular models [24], two-dimensional random polygon models, three-dimensional spherical models [25], three-dimensional ellipsoidal models [26], three-dimensional random convex polyhedral models [27–29], and non-convex polyhedral models [30]. Many scholars have conducted numerical simulations on HPC. For instance, Li et al. [31] studied the failure mode and process of HPC under uniaxial compression after ASR. Perkins et al. [32] examined the numerical simulation of HPC under high-strain-rate ballistic impacts, using the HJC model to capture the mechanical response of concrete targets. Osgouei et al. [33] analyzed the single-point and double-point bending performance of high-performance fiber-reinforced concrete beams through numerical simulation. Numerous scholars have also studied the fatigue characteristics of concrete through numerical simulations [34,35]. Pise et al. [36,37] developed a phenomenological material model to simulate the fractures within the HPC. This model could describe the nonlinear material behavior of both the HPC matrix and the fibers according to one-dimensional von Mises plasticity formulations and the Drucker–Prager plasticity, respectively.

However, there is a scarcity of studies on the deterioration process, mechanical properties, and interfacial transition zones of high-performance concrete (HPC) under ASR, especially over the course of several decades. In regions where ASR is significantly induced, it is crucial to investigate the deterioration and mechanical performance changes of HPC over extended periods of ASR.

This paper primarily investigates the axial compressive failure of HPC under ASR using experimental and numerical simulations. By altering the equivalent alkali content of the concrete's environment, the types of additives used, and the curing time, this study explores the degradation of its physical and mechanical properties and the patterns of failure. Additionally, a three-dimensional random aggregate model was used to simulate the failure of the concrete during compression failure.

2. Experimental Procedure

2.1. Raw Materials

(1) Cement

The cementitious material utilized in this study was P.II 52.5 cement, produced by the Gansu Qilian Mountains Cement Group Co., Ltd. (Lanzhou, China) The cement demonstrated adequate stability and conformance to physical and mechanical standards, the specifics of which are detailed in Table 1. The chemical composition and alkali-reactive components of the main raw materials are shown in Tables 2 and 3.

Table 1. Cement physical and mechanical properties.

No	Fineness/%	Specific Surface Area/$m^2 \cdot kg^{-1}$	Standard Consistency/%	Condensation Time/h		Flexural Strength/MPa		Compressive Strength/MPa	
				Initial Setting	Final Setting	3 d	28 d	3 d	28 d
P.II 52.5	0.8	412	25	1:35	2:26	5.6	9.3	26.8	57.2

Table 2. The chemical composition of the main raw materials (%).

Material	SiO_2	Al_2O_3	CaO	MgO	SO_3	Fe_2O_3	MnO	TiO_2	Na_2O	K_2O	I.L	Cl^-
P.II 52.5 Cement	19.56	3.78	65.88	2.42	2.41	3.69	—	—	0.50	0.82	0.94	0.022
SF	90.51	0.96	0.50	2.10	—	0.64	—	—	1.03	2.00	2.26	0.26
FA	52.68	32.42	2.94	1.21	0.74	7.47	—	—	0.74	1.46	0.34	0.0012
SG	26.09	26.88	37.38	5.6	1.75	0.67	—	—	0.49	0.83	0.31	0.014

Table 3. Alkali-active components of the main ingredients (%).

Material	K_2O	Na_2O	$Na_2O + 0.658\ K_2O$
P.II 52.5 cement	0.82	0.50	1.04
SF	1.35	0.63	1.52
FA	0.40	0.27	0.53
SG	2.00	1.03	2.35

(2) Fly Ash (FA)

The fly ash used in this study was a product of Gansu Yongdeng Lian Dian Fly Ash Co., Ltd. (Lanzhou, China), classified as Class I fly ash. The chemical composition of the fly ash is detailed in Table 3.

(3) Slag (SG):

The granulated blast furnace slag utilized in this study is the S95 grade product from Gansu Xiangyang Trading Co., Ltd.'s (Dingxi, China) mineral powder plant. The chemical composition of the slag is detailed in Table 3. The specific surface area of the slag is measured at 330 m^2/kg.

(4) Silica fume (SF):

The silica fume used in this study was a product of Qinghai Lantian Environmental Technology Co., Ltd. (Xining, China). It contained 90.51% SiO_2 and had a specific surface area of 26,200 m^2/kg. The chemical composition of the silica fume is detailed in Table 3.

(5) Fine aggregate: Sourced from the Ledu River in Qinghai, this river sand had a bulk density of 1639 kg/m^3 and a fineness modulus of 2.87, classified as moderate sand with a zone II grading. The specific performance indicators are listed in Table 4.

(6) Coarse aggregate: The granite-crushed stone from Xiaoxia in Xining had a maximum particle size of 20 mm and a flaky particle content of 2.6%, fitting a 5~20 continuous grading. The specific performance indicators are documented in Table 4. The 14-day rapid mortar bar test expansion rate was 0.007%, indicating no alkali-reactivity hazard.

(7) Superplasticizer: PJ-FDN polycarboxylic acid high-efficiency water reducer, a liquid product from Xining Yangjian Waterproof Additive Co., Ltd. (Xining, China), was recommended at a dosage of 1.5%, achieving a water reduction rate of over 25%.

(8) Air-entraining agent: Another product from Xining Yangjian Waterproof Additive Co., Ltd., this liquid agent was primarily composed of rosin thermopolymer, recommended at a dosage of 1.5%.

(9) Steel-reinforcement corrosion inhibitor: Also from Xining Yangjian Waterproof Additive Co., Ltd., this liquid additive mainly consists of calcium nitrite, with a 30% solid content, recommended at a 5% dosage.

Table 4. Basic parameters of aggregates.

	Apparent Density/(kg/m^3)	Bulk Density/(kg/m^3)	Porosity/%	Mud Content/%
Fine aggregate	2650	1470	38.1	5.6
Coarse aggregate		1530		

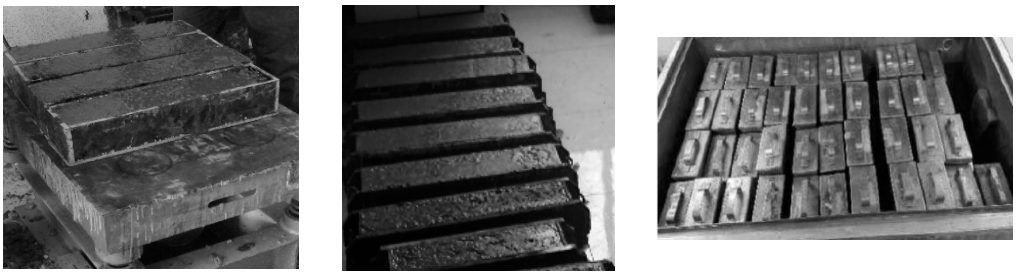
In this study, nine distinct concrete mixtures were designed, all of which shared the same strength grade. These mixtures were categorized based on three different admixture strategies: the addition of an air-entraining agent alone, the addition of a corrosion inhibitor alone, and the simultaneous addition of both air-entraining and corrosion-inhibiting agents. To explore how the equivalent alkali content affects the deterioration of physical and mechanical properties of concrete under high alkaline conditions, this study designed variants in equivalent alkali content based on three initial concrete mixtures. Specimens labeled as "-0" represent the material's original equivalent alkali content, assigned as the low alkali condition. By adding NaOH to the mixing water, the equivalent alkali content was increased. Specimens labeled "-1" are defined as the moderate alkali condition, and those labeled "-2" are defined as the high alkali condition. The detailed specifications of the equivalent alkali content and material usage for each mixture are provided in Table 5.

Table 5. Mixtures of concrete (kg/m^3).

No	Total	Cement	FA	SG	SF	Sand	Aggregate	Admixture-1	Admixture-2	Admixture-3	Water	Equivalent Alkali Content/%	Aggregate Volume/%
Ca50-0	500	325	60	100	15	741	1159		10	0.25	150	0.8	
Ca50-1	500	325	60	100	15	741	1159		10	0.25	150	1.3	
Ca50-2	500	325	60	100	15	741	1159		10	0.25	150	1.8	
C50Z-0	500	325	60	100	15	741	1159	33	10		127	0.8	
C50Z-1	500	325	60	100	15	741	1159	33	10		127	1.2	45
C50Z-2	500	325	60	100	15	741	1159	33	10		127	1.6	
Ca50Z-0	500	325	60	100	15	741	1159	33	10	0.25	127	0.8	
Ca50Z-1	500	325	60	100	15	741	1159	33	10	0.25	127	1.2	
Ca50Z-2	500	325	60	100	15	741	1159	33	10	0.25	127	1.6	

Note: Admixture-1 means rust inhibitors, admixture-2 means high-efficiency superplasticizer, admixture-3 means air-entraining agent.

In this experiment, a 1 mol/L NaOH solution was used, and all concrete specimens were fully immersed in the solution, as shown in Figure 1.



(**a**) Vibration (**b**) Demoulding (**c**) Soaking

Figure 1. The preparation process of concrete specimens. (**a**) Concrete is vibrated on a compactor, (**b**) concrete is demold from the mold, (**c**) concrete soaked in a high-alkaline solution.

2.2. Mechanical Performance Evaluation Indicators for Concrete

(1) Compressive strength

For this study, concrete specimens were immersed in a standard alkali solution and tested at intervals of 0 days, 28 days, 182 days, and 365 days using cubic specimens measuring 100 mm × 100 mm × 100 mm, which was started in November 2011. For the long-term test at 3650 days, specimens from the shorter side split after a flexural strength test were utilized. These were tested with two steel plates sized 100 mm × 100 mm × 10 mm placed on the specimen surfaces. The compressive strength of the concrete specimens can be expressed using Equation (1):

$$f_{cu} = \frac{F}{A} \tag{1}$$

where f_{cu} represents the compressive strength (MPa), F represents the load at failure (N), and A represents the compressed area (mm^2). The strength values measured using

non-standard specimens (100 mm × 100 mm × 100 mm) should be multiplied by a size conversion factor of 0.95 in GB/T 50081-2019 [38].

(2) Expansion rate

To evaluate the extent of length changes induced by ASR in concrete, a series of specimens measuring 515 mm × 100 mm × 100 mm are prepared. Stainless steel measurement probes, each 15 mm in length, were placed at both ends of each specimen, with an exposed portion of approximately 8 mm in GB50204-2015 [39]. The specimens were immersed for varying durations to measure length changes, and the expansion rate was calculated using Equation (2):

$$\varepsilon_t = \frac{L_t - L_0}{L_0 - 2\Delta} \tag{2}$$

where ε_t represents the expansion rate (%) of the specimen at t days of immersion, L_t denotes the length (mm) of the specimen at t days of immersion, L_0 is the reference length (mm) of the specimen, and Δ is the length (mm) of the probe exposed.

(3) Internal damage

In this study, it is assumed that the damage in the concrete is isotropic and that the Poisson's ratio does not change with the damage. Two opposite faces of the concrete specimen, each measuring 100 mm × 100 mm, are selected as the measurement surfaces. Along the diagonal of these measurement surfaces, transducers are placed at three positions to measure the ultrasonic pulse velocity V_t of the specimen.

The internal damage D_s [40] is calculated using Equation (3).

$$D_s = 1 - \frac{{V_t}^2}{{V_0}^2} \tag{3}$$

(4) Surface Damage

The surface damage layer detection is carried out using the one-sided flat measurement method in CECS 02-2005 [41], as shown in Figure 2. The surface of the component to be tested must be flat and in a naturally dry state. The 100 mm × 515 mm sides, top, and bottom surfaces of the concrete samples are selected as the flat measurement surfaces. On each flat measurement surface, eight pairs of measurement points are established, with distances between the inner edges of the two transducers set at 50, 100, 150, 200, 250, 300, 350, and 400 mm, respectively. During the test, the transmitting transducer is fixed at a specific position on the test surface, while the receiving transducer is moved at equal intervals to measure the ultrasonic propagation time at different distances.

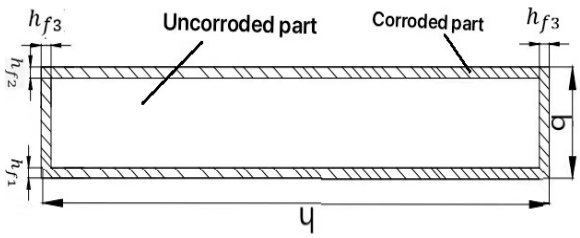


Figure 2. Surface damage layer of concrete.

The surface damage D_a is calculated using Equation (4).

$$D_a = 1 - \frac{A_{ht}}{A_{h0}} = 1 - \frac{\left(b - h_{f_1} - h_{f_2}\right)\left(h - 2h_{f_3}\right)}{bh} \tag{4}$$

where D_a represents the surface damage due to ASR; A_{h_0} represents the cross-sectional area of the concrete before ASR; A_{h_t} represents the initial cross-sectional area of the concrete

when ASR begins; b and h represent the width and height of the concrete specimen, respectively; h_{f_1}, h_{f_2}, and h_{f_3} represent the thickness of the corrosion damage layer on the top, bottom, and side surfaces of the concrete, respectively.

3. Results and Discussion

3.1. Impact of Corrosion Inhibitors and Air-Entraining Agents on Expansion Rate

The expansion rate serves as one of the crucial indicators for assessing the occurrence of ASR. To develop a model for the progression of ASR, several researchers have explored this from various perspectives, and the Kolmogorov–Avrami–Mehl–Johnson (KAMJ) [42] model is predominantly utilized. This model substitutes the reaction extent (the volumetric fraction of the phase change) with the expansion level of the sample to establish a kinetic relationship characterized by an S-shaped growth curve.

The equation is as follows:

$$\varepsilon_t = B \times \left\{1 + \varepsilon_{t_0} - \exp\left[-k(t - t_0)^M\right]\right\} \quad (5)$$

where ε_{t_0} and ε_t represent the expansion rates at initial t_0 and time t, respectively, with ε_{t_0} being 0 in this study; t_0 represents the first data collection point, which, for ease of presentation, is noted as 0.1 days, corresponding to $\varepsilon_{t_0} = 0$. t refers to the soaking time; B is the limit of the expansion rate for different mix ratios; k is the expansion rate constant affected by the formation and diffusion of the reaction products; and M is the Avrami exponent, which ranges between 0 and 4 and is considered a constant.

The alkaline reactivity of aggregates or cement is closely associated with the expansion rate constant k and the Avrami exponent M. With a constant M, higher values of the expansion rate constant lead to greater expansion rates; conversely, with a constant expansion rate constant k, higher Avrami exponents M result in greater expansion. Observation of the expansion rate development curves reveals variations in the rate of development across different periods. Therefore, by applying the first derivative to the Kolmogorov–Avrami–Mehl–Johnson (KAMJ) model, the expansion rate development speed curves for different soaking periods are obtained, as depicted in Figure 3.

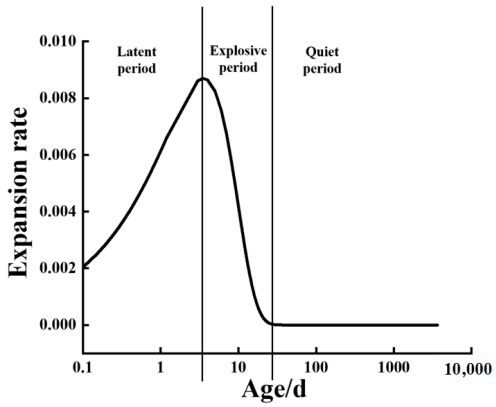
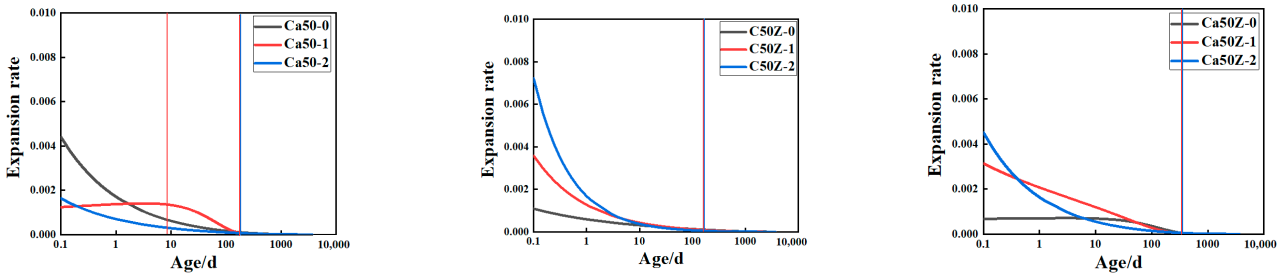


Figure 3. The rate of development of the KAMJ model.

The expansion rate reaches its peak between 5 and 7 days of soaking, a phase termed the "latent period", characterized by a short duration and a concave development pattern. After peaking, the expansion rate begins to decline, eventually approaching a near-zero minimum, marking this as the "explosive period", which exhibits a convex development. Once the minimal expansion rate is achieved, the "quiescent period" follows, which lasts longer and is characterized by a nearly horizontal trajectory, indicating a slope that is close to zero. Thus, the expansion rate development curve is divided into three distinct phases: concave development during the latent period, convex development during the explosive

period, and an overall S-shaped progression. Consequently, this study refers to the KAMJ model as the "flattened S-curve model".

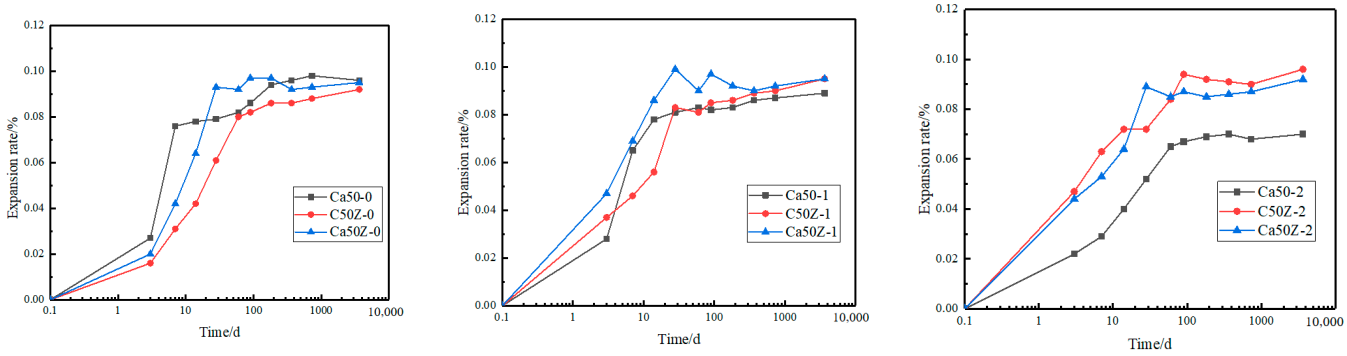
Figure 4 demonstrates that under long-term immersion in a standard alkali solution at 38 °C, HPC exhibits virtually no latent period and directly transitions into the explosive phase. This is attributed to the questionable alkali reactivity of the fine aggregates used in this study, along with the higher equivalent alkali content in the moderate and high alkali states of HPC, which causes the material to skip the latent period and enter the explosive phase at the onset of immersion. With the increase in the equivalent alkali content, the initial expansion rate also rises, suggesting that a higher alkali content accelerates the development rate of HPC expansion. However, the duration of the explosive phase remains consistent across different equivalent alkali contents at the same strength grade, indicating that the end timing of the explosive phase is not significantly influenced by the internal equivalent alkali content of the concrete.



(**a**) Ca50 (**b**) C50Z (**c**) Ca50Z

Figure 4. The development of expansion rate under long-term immersion in standard alkaline solution at 38 °C. (**a**) Ca50; (**b**) C50Z; (**c**) Ca50Z.

Figure 5 reveals that under low-alkali conditions, the specimens with only air-entraining agents exhibited a higher rate of expansion in the early stages of immersion. During the mid-immersion period, the specimens with both air-entraining agents and corrosion inhibitors reached the highest expansion rates, while those with only corrosion inhibitors maintained the lowest expansion rates across all the immersion times among the three admixture addition methods. In the moderate and high-alkali conditions, the specimens with only corrosion inhibitors and those with both air-entraining agents and corrosion inhibitors exhibited similar early expansion rates and values, whereas the specimens with only air-entraining agents consistently showed significantly lower expansion rates during all the immersion periods compared to the other two admixture strategies.



(**a**) Low equivalent alkali content (**b**) Moderate equivalent alkali content (**c**) High equivalent alkali content

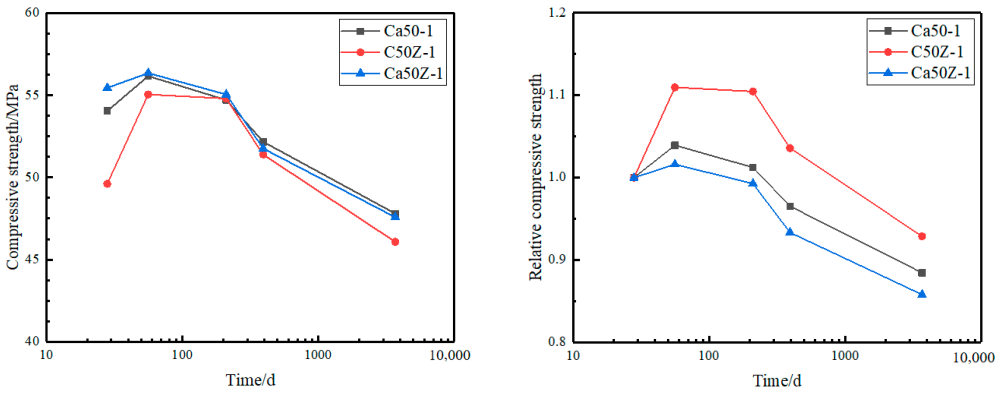
Figure 5. Influence of various additive application methods on the expansion rate of HPC. (**a**) Low; (**b**) moderate; (**c**) high.

It can be inferred from the study that under long-term ASR conditions, HPC with lower equivalent alkali content demonstrates the best resistance to ASR when only corrosion

inhibitors are added, with concrete specimens featuring both air-entraining agents, and corrosion inhibitors exhibiting similar expansion rate developments and peak values. Under conditions with higher equivalent alkali contents, the HPC with only air-entraining agents showed superior ASR resistance, maintaining consistently low expansion rates. Conversely, the specimens with only corrosion inhibitors and those with both air-entraining agents and corrosion inhibitors exhibited similar patterns in their expansion rate developments and peak values, both at higher levels. The simultaneous addition of both admixtures did not enhance the ASR resistance of the HPC; instead, the expansion rates were higher compared to the specimens with only one type of admixture added.

3.2. Influence of Immersion Duration in Standard Alkali Solution on the Compressive Strength of HPC

For the moderate alkali condition (-1), tests were conducted after soaking durations of 28 days, 182 days, and 365 days. The compressive strengths from these periods were divided by the initial compressive strength to calculate the relative compressive strengths $R_{cu,m}$, depicted in Figure 6. Due to the lengthy immersion times, the *x*-axis of the figure employs a logarithmic scale to clearly present the compressive strength across different soaking periods. The five datapoints for the various mix ratios in Figure 6 correspond to soaking periods of 0 days, 28 days, 182 days, 365 days, and 3650 days. The compressive strength after 28 days is noted as the strength at 0 days of soaking; hence, all five data points in the figure include an additional 28 days of curing time.



(**a**) Compressive strength (**b**) Relative compressive strength

Figure 6. Variations in the compressive strength and relative compressive strength of HPC under moderate alkaline conditions during different soaking periods. (**a**) Compressive strength; (**b**) relative compressive strength.

Figure 6 shows the compressive strengths of C50Z-1, Ca50-1, and Ca50Z-1 under immersion in standard alkali solution at 38 °C at intervals of 0 days, 28 days, 182 days, 365 days, and 3650 days. For C50Z-1, the compressive strengths were 49.61 MPa, 55.05 MPa, 54.8 MPa, 51.39 MPa, and 46.08 MPa, respectively; for Ca50-1, they were 54.04 MPa, 56.17 MPa, 54.71 MPa, 52.17 MPa, and 47.8 MPa, respectively; and for Ca50Z-1, they were 55.45 MPa, 56.35 MPa, 55.05 MPa, 51.76 MPa, and 47.58 MPa, respectively. The compressive strength of the HPC generally increased when soaked for 28 days compared to the initial compressive strength, followed by a decreasing trend after 182 days. The increase in strength observed in the first 100 days of exposure to an aggressive environment is possibly associated with the accumulation of the products of interactions between the cement stone and the aggressive environment, which is convincingly shown in reference [43]. This indicates that the compressive strength of HPC immersed in standard alkali solution at 38 °C for a year undergoes an initial increase followed by a decline. The compressive strength of most mixtures reaches its peak after the 28-day immersion treatment, subsequently showing a continual decrease. The reduction in compressive strength from its peak to the

values observed after 10 years of immersion is calculated as 16.29%, 14.90%, and 15.56% for C50Z, Ca50, and Ca50Z, respectively.

Calculations of the decrease in compressive strength of HPC after one year and ten years of immersion reveal that the rate of decline in compressive strength over the first year exceeds that over ten years across all the mixtures. This phenomenon correlates with the expansion rate progression; specifically, the rapid increase in expansion rate within the first year of immersion in standard alkali solution leads to extensive internal cracking in the concrete, thereby accelerating the reduction in compressive strength.

The relationship between the relative compressive strength of HPC across the different durations of immersion under long-term ASR conditions can be described using a second-order linear relationship, as shown in Equation (6). However, the coefficients of the linear relationship vary among the different mixtures, as summarized in Table 6. This formula allows for the prediction of compressive strength at various stages of ASR based on the initial compressive strength of the HPC.

$$R_{cu,m} = q_1\left\{\left[\log_{10}(t+28)\right]^2 + p_1\left[\log_{10}(t+28)\right]\right\} + z_1 \quad (6)$$

Table 6. Coefficients for the relationship between compressive strength and soaking time of HPC under standard alkali solution immersion at 38 °C.

Mixture	q_1	p_1	z_1	R
C50Z	−0.129	0.603	0.412	0.9
Ca50	−0.056	0.221	0.793	0.99
Ca50Z	−0.04	0.127	0.904	0.96

Note: The critical correlation coefficient at a significance level of 0.05 with 5 degrees of freedom is 0.75.

3.3. Impact of Equivalent Alkali Content on the Compressive Strength of HPC after 10 Years of Immersion in Standard Alkali Solution

Figure 7 illustrates the compressive strengths of HPC after 10 years of immersion at different equivalent alkali contents. This clearly shows that the specimens in the low-alkali state (-0) exhibited the highest compressive strength among the three evaluated alkali content levels, and there was a consistent decline in compressive strength as the equivalent alkali content increased. The reduction in compressive strength in the moderate alkali state compared to the low-alkali state was within 5%, while in the high-alkali state, it was within 12%. These data indicate that an increase in equivalent alkali content leads to a progressively greater reduction in the compressive strength of HPC under long-term ASR conditions.

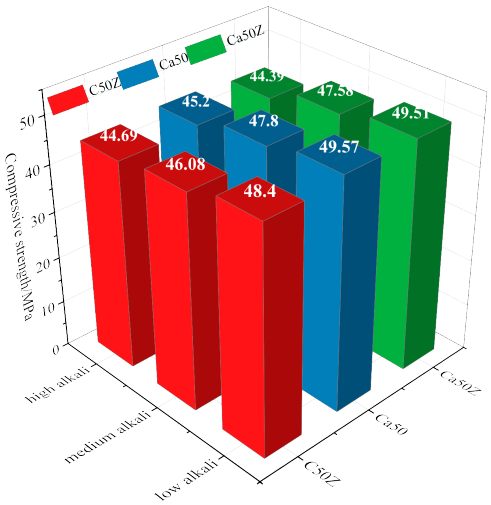
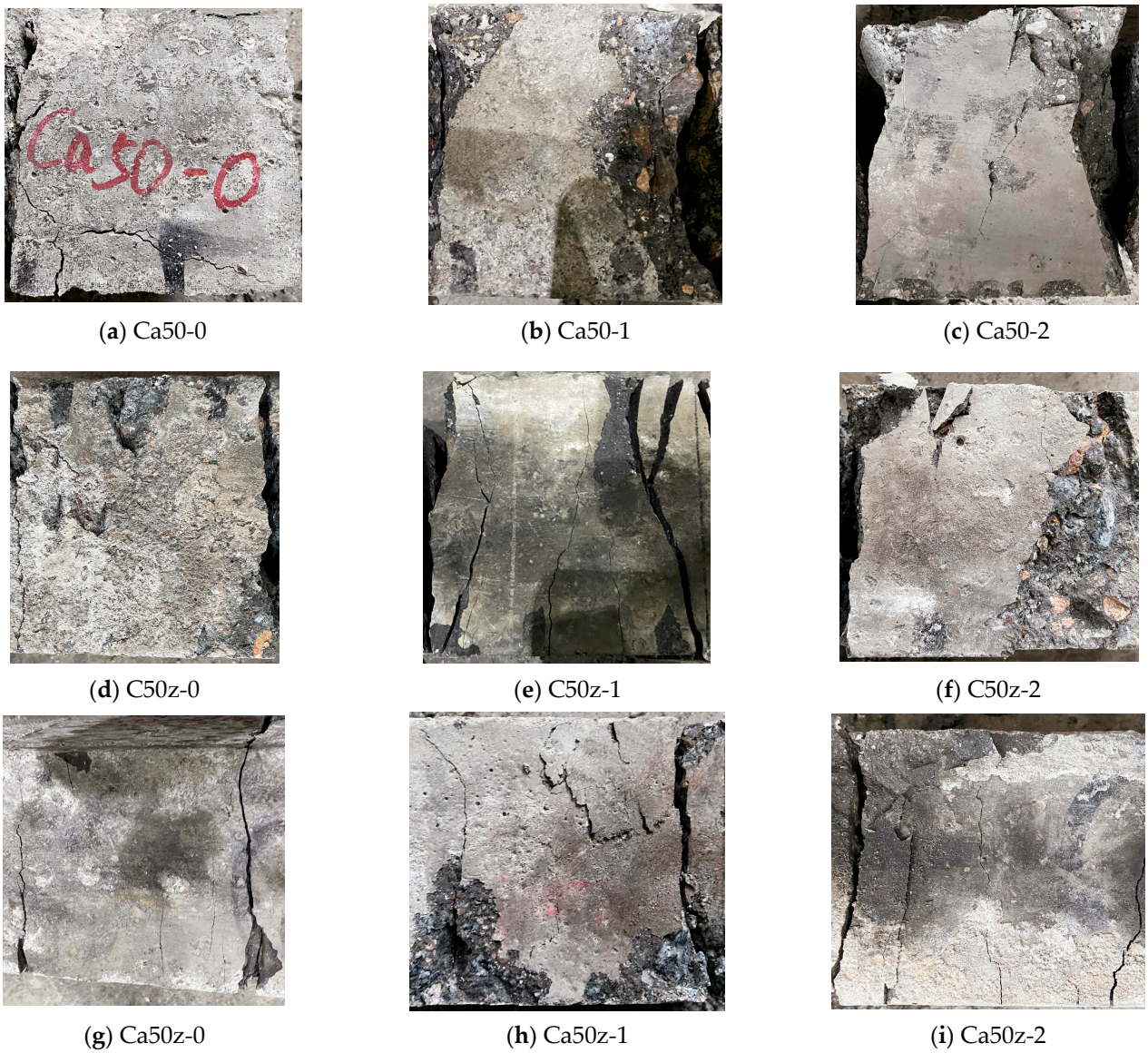


Figure 7. The influence of equivalent alkali content on the compressive strength of HPC.

3.4. Analysis of Failure Modes

Figure 8 shows the damage patterns of HPC under different conditions. It can be seen that as the equivalent alkali content increases, the damage morphology of the specimens becomes more severe. At the lowest alkali content, the surface of the specimens remains relatively intact with few cracks. As the alkali content increases, extensive spalling and a greater number of wider cracks appear on the specimen surfaces, with the similar damage mode of OPC. At high alkali levels, the characteristics of the damage are similar to those at moderate alkali levels, except for variations in surface spalling. It is also observable from the figure that under high alkali conditions, specimens with a single additive exhibit more severe damage, whereas those with two additives, like Ca50z, show relatively less damage.



(**a**) Ca50-0 (**b**) Ca50-1 (**c**) Ca50-2

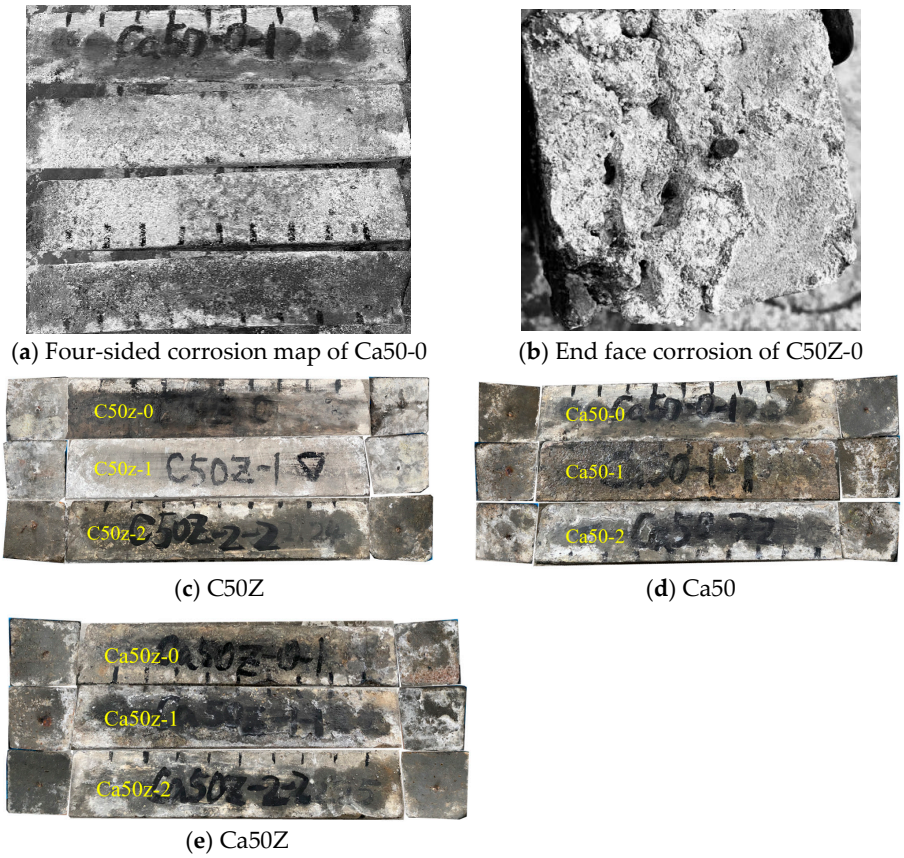
(**d**) C50z-0 (**e**) C50z-1 (**f**) C50z-2

(**g**) Ca50z-0 (**h**) Ca50z-1 (**i**) Ca50z-2

Figure 8. Failure modes of HPC under various working conditions.

After long-term immersion in standard alkali solution, all the groups of specimens exhibited phenomena such as peeling of the surface mortar layer, detachment of fine aggregates, and exposure of coarse aggregates, as shown in Figure 9. In severely damaged specimens, end-face corrosion defects appeared on the concrete surface, as depicted in Figure 9. No typical features of ASR damage, such as map cracking, were observed on

the surfaces of the specimens, indicating that the phenomenon of ASR damage is not pronounced in HPC under long-term conditions.



(**a**) Four-sided corrosion map of Ca50-0 (**b**) End face corrosion of C50Z-0

(**c**) C50Z (**d**) Ca50

(**e**) Ca50Z

Figure 9. Corrosion of HPC specimens in different alkaline environments.

3.5. Impact of Equivalent Alkali Content on Internal Damage Variables in HPC after 10 Years of Immersion in Standard Alkali Solution

The influence of the equivalent alkali content on internal damage variables in HPC under long-term ASR conditions is shown in Figure 10.

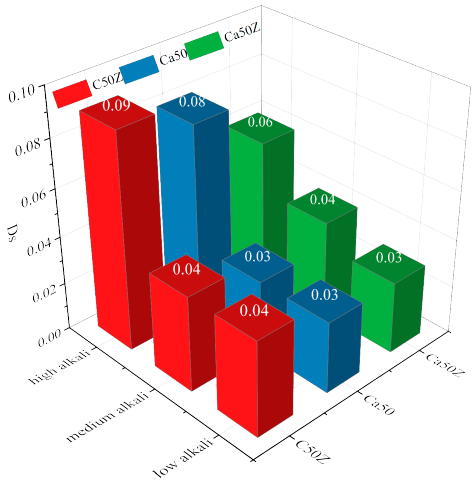
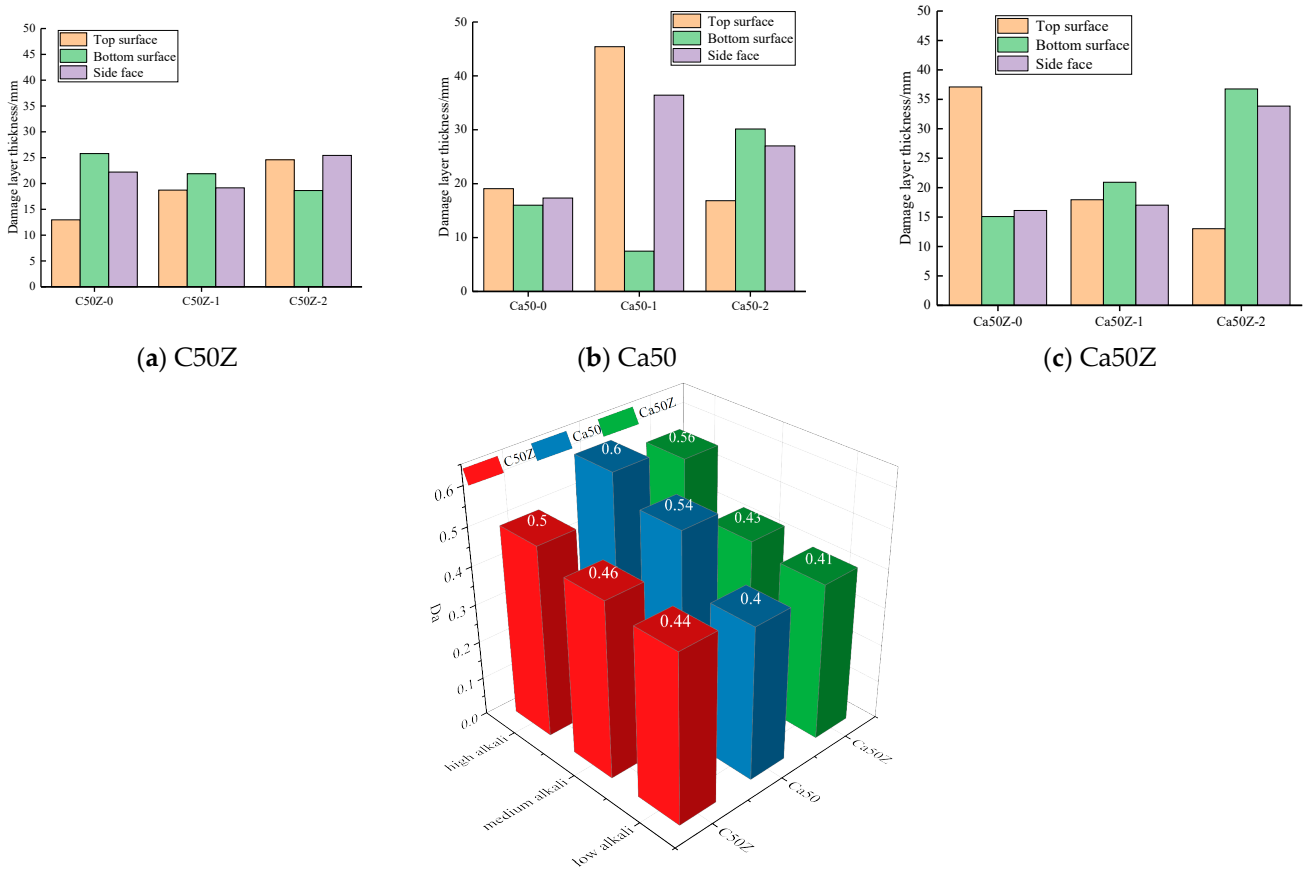


Figure 10. Influence of equivalent alkali content on internal damage variables in HPC under long-term ASR conditions.

As shown in Figure 10, the internal damage variables increase with the rise in equivalent alkali content. C-The calculations indicate that for the moderate and high-alkali conditions compared to the low-alkali condition, the increments in internal damage variables for mixtures C50Z-1, Ca50-1, and Ca50Z-1 are 10.00%, 0.00%, and 33.33%, respectively; for C50Z-2, Ca50-2, and Ca50Z-2, the increments are 125.00%, 166.67%, and 100.00%, respectively. These results demonstrate that in a high-alkaline environment, the specimens with two different admixtures show the least internal damage, whereas specimens with any single admixture see more than a doubling of internal damage value, suggesting that the combined effects of the two admixtures can suppress the diffusion of chloride ions within the specimens under high alkalinity. Conversely, in a moderate alkaline environment, the increase in internal damage variables is relatively low across all three admixture strategies.

Figure 11 reveals that after 10 years of immersion in a standard alkali solution, the thickness of the damage layer on the bottom surfaces of the HPC specimens is comparatively large, indicating that long-term ASR causes significant cracking and severe corrosion by the alkali solution on the bottom surfaces. Conversely, the patterns of damage layer thickness on the top and side surfaces vary with different mixtures and equivalent alkali contents. Under low-alkali conditions, the damage layer thickness on the top surface is greater than on the side surfaces; this pattern persists in moderate-alkali conditions. However, in high-alkali conditions, the side surfaces exhibit a thicker damage layer compared to the top surface. Thus, it can be concluded that the bottom surface of HPC suffers the most severe damage under long-term ASR conditions. Additionally, in low- and moderate-alkali conditions, the top surface damage is more severe than the side surface damage, whereas in high-alkali conditions, the side surface damage exceeds that on the top.



(**a**) C50Z (**b**) Ca50 (**c**) Ca50Z

(**d**) The relationship between surface damage and equivalent alkali content

Figure 11. The thickness distribution of the four surface damage layers of HPC and the relationship between the degree of surface damage and the equivalent alkali content.

To investigate whether there is a correlation between internal damage variables and surface damage variables under long-term ASR conditions, data for both types of damage variables were collectively analyzed and are presented in Figure 12. The relationship between these two damage variables was subsequently determined and is described in Equation (7).

$$D_a = 0.11 \times \ln D_s + 0.81 \; R = 0.73 \tag{7}$$

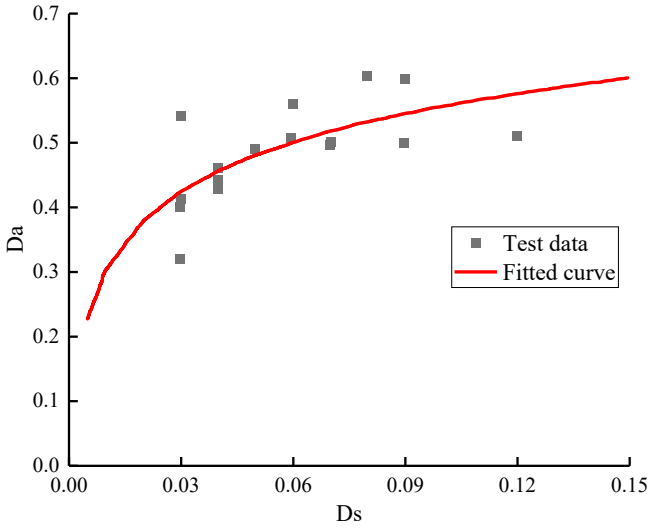


Figure 12. The relationship between internal damage and superficial damage.

4. Numerical Simulation of Mechanical Properties in Concrete Cubes under Uniaxial Compression

This study utilizes a three-dimensional microscale model of concrete, implemented in ANSYS 17.0 software and coded in Fortran, to perform numerical simulations of the uniaxial compression behavior of concrete cubes. It examines the failure patterns and processes within the coarse and fine aggregates, the interfacial transition zone (ITZ), and the surrounding cement matrix under load. This research corroborates the link between macroscopic and microscopic mechanical properties, affirming the micro-mechanical analyses presented in the second chapter.

4.1. The Process of Establishing a Three-Dimensional Random Aggregate Model

Drawing on the principles of micro-mechanics and concrete damage mechanics, concrete is categorized into three distinct phases: aggregates, mortar, and the ITZ. Building on this conceptual framework, a microscopic model of concrete has been developed. Researchers from around the world have suggested various two-dimensional shapes and geometric configurations for modeling aggregates. To accurately depict the real structure of aggregates, Fang et.al. [21] proposed a reconstruction method for a concrete three-phase moderate-scale model based on Voronoi tessellation. This paper adopts a three-dimensional random micro-finite element model to simulate the spatial random characteristics of fragmented aggregates.

In the designated methodology, aggregates with diameters ranging from 8 mm to 23 mm are systematically embedded within a cubic domain of 100 mm per edge, achieving an aggregate volume fraction of 45%. Using the generated three-dimensional random aggregate model, the microscopic finite element mesh of the concrete is created using a mapping grid division algorithm. Subsequently, the corresponding material identification algorithm is employed [44], and the spatial relationships between different grids and aggregate model units are determined to establish the spatial positions of various microscopic components (aggregates, mortar, and ITZ), resulting in the final microscopic concrete model. During this process, the hexahedral element mesh size is set to 1 mm, ensuring that its size is close to 1/8 to 1/4 of the minimum aggregate size, which can not only improve the calculation

efficiency but also reduce the calculation time [45]. Figure 13 illustrates the construction process of a three-dimensional random aggregate model, resulting in a cubic model with a side length of 100 mm. Local mesh division was utilized to segment the model into two major sections: one defined by the thickness of the surface damage, and the other comprising the core area where no damage occurred.

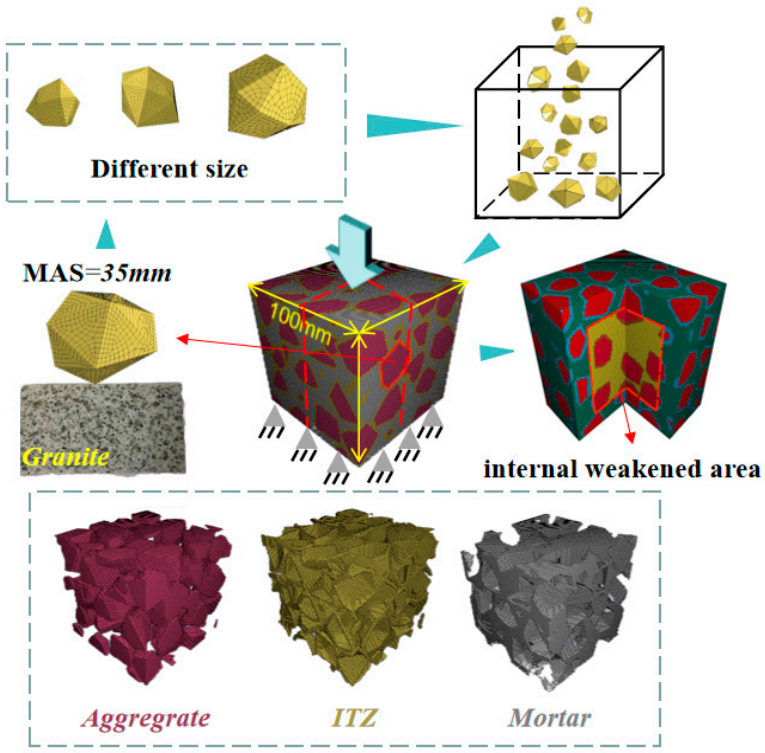


Figure 13. The process of generating a three-dimensional random aggregate model.

4.2. Material Parameter Determination

To simulate the uniaxial compressive mechanical behavior of the concrete cubic specimens, and considering the microscopic mechanical properties of the concrete aggregates, mortar, and the ITZ, this study adopts the *MAT JOHNSON HOLMQUIST CONCRETE (HJC) [46] material model from LS-DYNA as the aggregate model and *MAT CONCRETE DAMAGE REL3 (K&C) [47] as the mortar and ITZ model. As noted by Wu et al. [48], the automatic parameter generation for the K&C model is convenient. It only needs to input the density, Poisson's ratio, uniaxial compressive strength, and pressure–strain rate enhancement coefficient curve of concrete as initial parameters.

Regarding the mechanical properties of the mortar, relevant parameters can be obtained through microhardness and other mechanical performance experiments [49]. The ITZ bond splitting strength was estimated from the obtained ITZ microhardness results, which was used to calculate the ITZ compressive strength $f_{m,cu(ITZ)}$. Some scholars also believe that the performance of ITZ can be assumed to be 80% of the mortar performance [50], as shown in Table 7. In this study, low-alkali reactive aggregates were used for long-term immersion in alkali solution, and their influence was neglected. In comparison to KC, the HJC material model relies on the material strength. The experimental measurements yielded a gravel density (ρ) ranging from 2648 to 2680 kg·m^{-3} and a compressive strength (f_c) of 110 to 128 MPa.

Table 7. K&C material model parameters.

Number	ρ(mor)/kg·m^{-3} [31]	$f_{m,cu(mor)}$/MPa	$E_{c(mor)}$/MPa	ρ(ITZ)/kg·m^{-3}	$f_{m,cu(ITZ)}$/MPa	$E_{c(ITZ)}$/MPa
Ca50-0	2500/2550	7.0	27.7	2500/2550	16.3	7.3
Ca50-1	2500/2550	7.0	27.6	2500/2550	16.2	7.2
Ca50-2	2500/2550	6.7	27.0	2500/2550	12.9	6.3

4.3. Comparative Analysis of Numerical Simulation Results and Experimental Findings

A three-dimensional random micro-finite element model was employed in this research to conduct numerical simulations examining the static uniaxial compression behavior of three concrete mixtures: Ca50-0, Ca50-1, and Ca50-2. The objective of this study was to forecast the variations in compressive strength of HPC following a decade of ASR corrosion. Predictive outcomes from these simulations were subsequently juxtaposed with empirical data, facilitating a detailed examination of the failure morphology and its progression.

Experimental and numerical simulation comparative analyses were carried out. Based on the stress–strain curves obtained through numerical simulation, it is evident that the peak stresses for Ca50-0, Ca50-1, and Ca50-2 exhibit discrepancies when compared to the experimental results, as shown in Figure 14. The respective errors are +7.6%, +0.6%, and −3.1%. The overall errors are relatively small, which could be attributed to potential systematic or incidental errors in the experimental setup. The primary model material parameters were derived through fitted relationships, which might introduce computational errors.

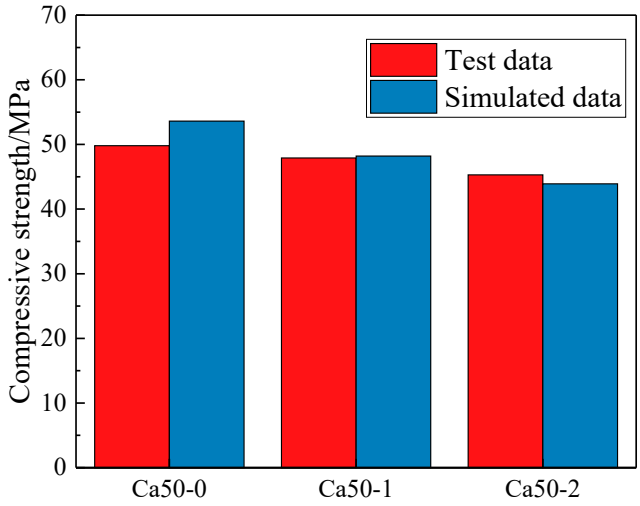


Figure 14. Comparison of cube uniaxial compression mechanical property test results with simulation results.

Overall, these findings indicate the reliability of this model for numerical simulations of concrete cubic uniaxial compression behavior.

4.4. Analysis of Failure Process

The graphical representation in Figure 15 illustrates the progressive failure over time for the Ca50-0, Ca50-1, and Ca50-2 micro-models after loading. To examine the varying failure states at different time intervals, analysis was conducted at 10 μs, 15 μs, 20 μs, 25 μs, and 40 μs. The mechanical properties of the external weakened regions of the model continuously deteriorate with increasing equivalent alkali contents. Numerical simulations reveal that higher alkali contents lead to more severe damage in the models. Figure 15 illustrates the damage processes in the 3/4 and 1/2 models, providing a clearer view of the failure modes within the concrete. At 10 μs, surface cracks are already observable in Ca50-2, resulting from internal fractures caused by surface layer corrosion, which facilitate

the formation of cracks. By 15 µs, surface cracks begin to appear on Ca50-0, with more severe damage observed in Ca50-2, where the interfacial transition zone (ITZ) around the aggregates shows significant destruction, typically presenting diagonal cracks. A cross-sectional observation over time reveals that, regardless of the equivalent alkali content, damage initially occurs on the surface. From the damage diagram of Ca50-2, it is evident that regions of internal performance change, which occur following surface corrosion by the alkali environment, are the primary sites of subsequent damage. Numerous cracks within the specimen occur at the interface between mortar and aggregate, an area inherently weaker and more susceptible to microfracturing under alkali corrosion, thereby facilitating the propagation of cracks. By 40 µs, a primary crack propagated from the surface, extending throughout and reaching the base, displaying pronounced splitting failure.

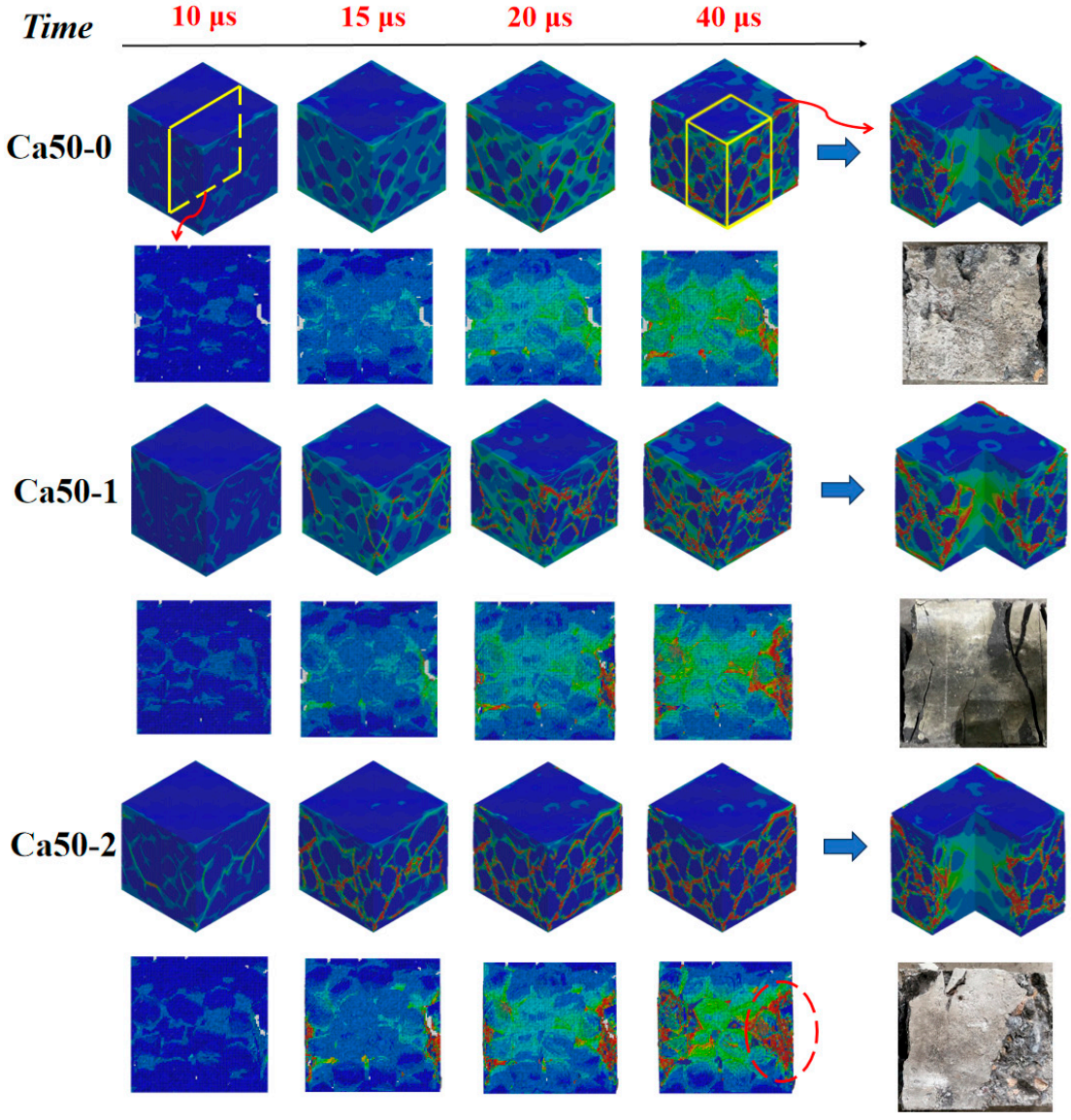


Figure 15. Mesoscopic failure process of Ca50.

Comparing the images of the experimental specimens with the failure progression depicted in the figure, a notable congruence is observed between the observed failure mechanisms and those simulated by the model, thus validating the fidelity of the micro-scale simulation.

At the microscale level, concrete is composed of aggregates, mortar, and the ITZ, each displaying distinct mechanical characteristics. An exploration of the mechanical properties

of these components under uniaxial compression is essential to understand the overall macroscopic mechanical properties of concrete. In Figure 16, which features mixture Ca50z-1, the failure morphology and progression of aggregates, mortar, and ITZ are depicted at specific time points: 10 μs, 15 μs, 20 μs, 25 μs, and 40 μs. Minimal damage to the aggregates and localized failure, mainly in the central region of the mortar, are observed under the load. The most extensive damage is sustained by the ITZ, positioned at the edges of the aggregates, underscoring its role as a critical transitional area between the aggregates and the mortar. By 15 μs, minor strains are noticeable in the center of the mortar and ITZ, with notably higher strain levels in the ITZ due to its comparatively weaker mechanical properties. Initial damage occurs primarily within the mortar, intensifying at the interfaces. As the simulation progresses, cracks develop and merge. By 40 μs, the ITZ is substantially compromised, confirming it as the weakest region within the concrete structure.

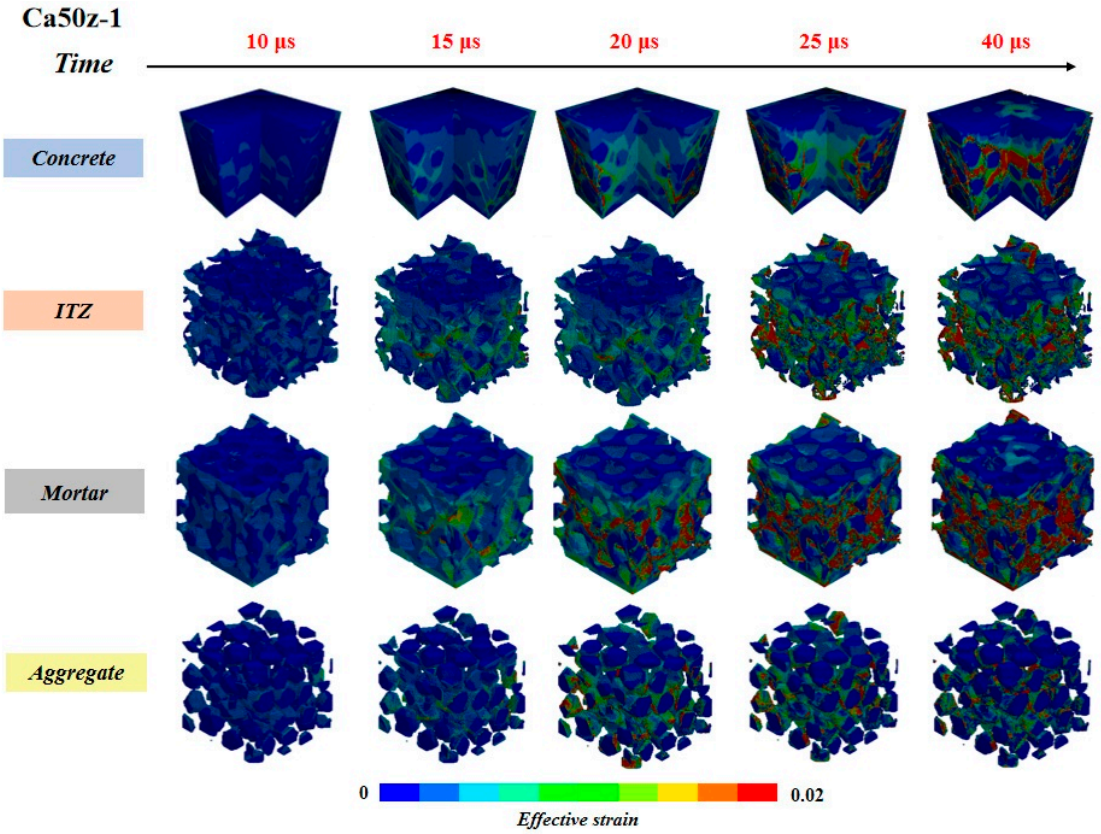


Figure 16. The failure process of each component of concrete.

5. Conclusions

The study investigates the effects of long-term (10 years) ASR on the uniaxial compression test, microscopic mechanics, and the three-dimensional random aggregate concrete microscopic model of HPC. The following conclusions are drawn:

(1) The expansion rate could be calculated based on the early expansion rate, with a difference of nearly 0.1% compared to the 1-year expansion rate. HPC with only rust inhibitors had the lowest expansion rate in low-alkali conditions, while HPC with only air entraining agents had the lowest expansion rate in medium- to high-alkali conditions.

(2) With long-term exposure to ASR, the compressive strength of HPC exhibits an initial increase followed by a decreasing trend. The relationship between compressive strength and soaking time was established to predict the compressive strength of HPC at different stages under the action of ASR.

(3) Under long-term ASR inhibition measures, the internal damage of HPC was relatively minor, but surface damage was more severe. The patterns of internal and surface damage concerning concrete equivalent alkali content and additive addition methods were consistent with the expansion rate. Additionally, a relationship between internal and surface damage was established.

(4) A three-dimensional random aggregate concrete microscopic model was constructed. The results indicated a consistent match between simulated failure patterns and experimental outcomes, affirming the reliability of the three-dimensional random aggregate concrete microscopic model in simulating the uniaxial compression behavior of HPC subjected to long-term ASR corrosion.

6. Recommendations

The impact of ASR on the durability of concrete is a significant research focus in the field of civil engineering, both domestically and internationally. Investigating the changes in the durability of high-performance concrete with inhibitory measures under ASR is particularly important for reducing the occurrence and effects of ASR. This study suggests that future research can be conducted at the component and structural levels of concrete. Additionally, employing methods such as CT scanning can allow for the observation of internal crack formation without damaging the structure, further elucidating the mechanisms of ASR.

Author Contributions: Conceptualization, J.G. (Juan Guo); Methodology, J.G. (Juan Guo), J.G. (Jianbo Guo) and J.Z.; Software, J.G. (Jianbo Guo) and J.Z.; Validation, J.G. (Jianbo Guo), H.Y., H.M., J.Z. and L.Z.; Formal analysis, H.M. and J.Y.; Investigation, J.G. (Jianbo Guo), J.Z., J.Y., F.W. and L.Z.; Resources, F.W.; Data curation, J.G. (Juan Guo), J.G. (Jianbo Guo), H.M., J.Y. and F.W.; Writing—original draft, J.G. (Juan Guo), J.G. (Jianbo Guo) and J.Y.; Writing—review & editing, J.G. (Jianbo Guo), H.M., F.W. and L.Z.; Visualization, H.Y.; Supervision, H.Y., H.M., J.Z. and L.Z.; Project administration, H.Y.; Funding acquisition, H.Y. All authors have read and agreed to the published version of the manuscript.

Funding: This research was funded by National Natural Science Foundation of China (52178190). The National Basic Research Program of China (973 Program) funded Project (2015CB655102) and Qinghai Provincial Science and Technology Support Plan (2013-G-Q006A).

Data Availability Statement: The data presented in this study are available from the corresponding author upon request (for ethical reasons).

Conflicts of Interest: The authors declare that they have no conflicts of interest.

References

1. Peng, Z.; Shi, C.; Shi, Z.; Lu, B.; Wan, S.; Zhang, Z.; Chang, J.; Zhang, T. Alkali-aggregate reaction in recycled aggregate concrete. *J. Clean. Prod.* **2020**, *255*, 120238. [CrossRef]
2. Rasheed, P.A.; Nayar, S.K.; Barsoum, I.; Alfantazi, A. Degradation of concrete structures in nuclear power plants: A review of the major causes and possible preventive measures. *Energies* **2022**, *15*, 8011. [CrossRef]
3. Yang, G.; Zhao, J.; Wang, Y. Durability properties of sustainable alkali-activated cementitious materials as marine engineering material: A review. *Mater. Today Sustain.* **2022**, *17*, 100099. [CrossRef]
4. Dai, X.; Aydin, S.; Yardimci, M.Y.; Lesage, K.; de Schutter, G. Influence of water to binder ratio on the rheology and structural Build-up of Alkali-Activated Slag/Fly ash mixtures. *Constr. Build. Mater.* **2020**, *264*, 120253. [CrossRef]
5. Marko, M.; Hrubý, P.; Janča, M.; Křikala, J.; Hajzler, J.; Šoukal, F.; Vojtíšek, J.; Doležal, M. Monitoring of Ion Mobility in the Cement Matrix to Establish Sensitivity to the ASR Caused by External Sources. *Materials* **2022**, *15*, 4730. [CrossRef] [PubMed]
6. McCoy, W.J.; Caldwell, A.G. New approach to inhibiting alkali-aggregate reaction expansion. *J. Proc.* **1951**, *22*, 693–706.
7. Dai, X.; Aydın, S.; Yardımcı, M.Y.; Lesage, K.; De Schutter, G. Effects of activator properties and GGBFS/FA ratio on the structural build-up and rheology of AAC. *Cem. Concr. Res.* **2020**, *138*, 106253. [CrossRef]
8. Shayan, A.; Ivanusec, I. Influence of NaOH on mechanical properties of cement paste and mortar with and without reactive aggregate. In Proceedings of the 8th International Conference on Alkali-Aggregate Reaction, Kyoto, Japan, 17–20 July 1989; Society of Materials Sciences: Kyoto, Japan, 1989; pp. 715–772.
9. Dai, X.; Aydin, S.; Yardimci, M.Y.; Qiang, R.; Lesage, K.; De Schutter, G. Rheology, early-age hydration and microstructure of alkali-activated GGBFS-Fly ash-limestone mixtures. *Cem. Concr. Compos.* **2021**, *124*, 104244. [CrossRef]

10. Cavalcanti, A.J.C.T. Alkali-aggregate reaction at Moxoto dam, Brazil. In Proceedings of the 7th International Conference on Alkali-Aggregate Reaction in Concrete, Ottawa City, ON, Canada, 1986; pp. 168–172. Available online: https://icaarconcrete.org/icaar-7/ (accessed on 24 June 2024).
11. Sanchez, L.F.M. Contribution to the Assessment of Damage in Aging Concrete Infrastructures Affected by Alkali-Aggregate Reaction. Ph.D. Thesis, Department of Geology and Geological Engineering, Université Laval, Québec, QC, Canada, 2014.
12. Nixon, P.J.; Bollinghaus, R. The effect of alkali aggregate reaction on the tensile and compressive strength of concrete. *Durab. Build. Mater.* **1985**, *2*, 243–248.
13. Giaccio, G.; Zerbino, R.; Ponce, J.M.; Batic, O. Mechanical behavior of concretes damaged by alkali-silica reaction. *Cem. Concr. Res.* **2008**, *38*, 993–1004. [CrossRef]
14. Dai, X.; Aydın, S.; Yardımcı, M.Y.; Lesage, K.; De Schutter, G. Rheology and microstructure of alkali-activated slag cements produced with silica fume activator. *Cem. Concr. Compos.* **2022**, *125*, 104303. [CrossRef]
15. Dai, X.; Aydin, S.; Yardimci, M.Y.; De Schutter, G. Rheology and structural build-up of sodium silicate-and sodium hydroxide-activated GGBFS mixtures. *Cem. Concr. Compos.* **2022**, *131*, 104570. [CrossRef]
16. Feng, J.; Chua, S.X.; Yang, F.; Qian, S. Crack repairing of high strength engineered cementitious composites using bacteria-free waste medium. *Cem. Concr. Compos.* **2021**, *123*, 104203. [CrossRef]
17. Marzouk, H.; Langdon, S. The effect of alkali-aggregate reactivity on the mechanical properties of high and normal strength concrete. *Cem. Concr. Compos.* **2003**, *25*, 549–556. [CrossRef]
18. Fares, G.; Khan, M.I. HPC composites formulated to counteract early ASR expansion. *J. Mater. Civ. Eng.* **2013**, *25*, 1951–1958. [CrossRef]
19. Agioutantis, Z.; Stiakakis, C.; Kleftakis, S. Numerical simulation of the mechanical behaviour of epoxy based mortars under compressive loads. *Comput. Struct.* **2002**, *80*, 2071–2084. [CrossRef]
20. Fang, Q.; Zhang, J. 3D numerical modeling of projectile penetration into rock-rubble overlays accounting for random distribution of rock-rubble. *Int. J. Impact Eng.* **2014**, *63*, 118–128. [CrossRef]
21. Fang, Q.; Zhang, J.; Zhang, Y.; Wu, H.; Gong, Z. A 3D mesoscopic model for the closed-cell metallic foams subjected to static and dynamic loadings. *Int. J. Impact Eng.* **2015**, *82*, 103–112. [CrossRef]
22. Guo, J.; Zhang, J.; Yu, H.; Ma, H.; Wu, Z. Experimental and 3D mesoscopic investigation of uniaxial compression performance on basic magnesium sulfate cement-coral aggregate concrete (BMSC-CAC). *Compos. Part B: Eng.* **2022**, *236*, 109760. [CrossRef]
23. Guo, J.; Zhang, J.; Ma, H.; Yu, H.; Wu, Z.; Han, W.; Liu, T. Dynamic behavior of a new type of coral aggregate concrete: Experimental and numerical investigation. *J. Mater. Civ. Eng.* **2023**, *35*, 04023124. [CrossRef]
24. Saksala, T. Numerical modelling of concrete fracture processes under dynamic loading: Meso-mechanical approach based on embedded discontinuity finite elements. *Eng. Fract. Mech.* **2018**, *201*, 282–297. [CrossRef]
25. Potapov, S.; Masurel, A.; Marin, P.; Daudeville, L. Mixed DEM/FEM modeling of advanced damage in reinforced concrete structures. *J. Eng. Mech.* **2017**, *143*, 04016110. [CrossRef]
26. Fang, Q.; Zhang, J.; Zhang, Y.; Gong, Z.; Chen, L.; Liu, J. 3D numerical investigation of cement mortar with microscopic defects at high strain rates. *J. Mater. Civ. Eng.* **2016**, *28*, 04015155. [CrossRef]
27. Guo, J.; Zhang, J.; Yu, H.; Ma, H. Dynamic compressive behaviour of basic magnesium sulfate cement–coral aggregate concrete (BMSC–CAC) after exposure to elevated temperatures: Experimental and analytical studies. *Constr. Build. Mater.* **2023**, *382*, 131336. [CrossRef]
28. Ma, H.; Wu, Z.; Yu, H.; Zhang, J.; Yue, C. Experimental and three-dimensional mesoscopic investigation of coral aggregate concrete under dynamic splitting-tensile loading. *Mater. Struct.* **2020**, *53*, 12. [CrossRef]
29. Ma, H.; Guo, J.; Liu, T.; Yu, H.; Zhang, J.; Wu, Z.; Yue, C.; Mei, Q. Experimental and numerical studies on the mechanical behaviors of basic magnesium sulfate cement concrete under dynamic split-tension. *J. Build. Eng.* **2023**, *77*, 107525. [CrossRef]
30. Jia, M.; Xu, W.; Zhu, Z. Numerical study on the excluded volumes of realistic 3D non-convex particles. *Powder Technol.* **2019**, *349*, 52–58. [CrossRef]
31. Li, L.; Ma, H.; Yu, H.; Zhang, J.; Cheng, M.; Wu, Z.; Yan, J.; Zhang, L.; Fan, H.; Wang, F. Attack resistance mechanism, uniaxial compressive mechanical properties and meso-simulation of high-performance concrete exposed to brine in salt lake for 10 years. *Constr. Build. Mater.* **2023**, *407*, 133520. [CrossRef]
32. Perkins, R.A.; Duncan, C.J.; Johnson, D.; Stone, T.W.; Sherburn, J.A.; Chandler, M.; Moser, R.D.; Paliwal, B.; Prabhu, R.K.; Hammi, Y. Assessment of a high strength concrete using experimental and numerical methodologies for high strain rate ballistic impacts. *Int. J. Impact Eng.* **2023**, *178*, 104598. [CrossRef]
33. Osgouei, Y.B.; Tafreshi, S.T.; Pourbaba, M. Experimental and Numerical Characterization of Non-Proprietary UHPFRC Beam—Parametric Analyses of Mechanical Properties. *Buildings* **2023**, *13*, 1565. [CrossRef]
34. Tomann, C.; Lohaus, L.; Aldakheel, F.; Wriggers, P. Influence of water-induced damage mechanisms on the fatigue deterioration of high-strength concrete. In Proceedings of the Fib Symposium, Krakow, Poland, 27–29 May 2019; pp. 1944–1951.
35. Wriggers, P.; Aldakheel, F.; Lohaus, L.; Heist, M. Water-induced damage mechanisms of cyclically loaded high-performance concretes. *Bauingenieur* **2020**, *95*, 126–132. [CrossRef]
36. Pise, M.; Brands, D.; Schröder, J. Development and Calibration of a Phenomenological Material Model for Steel-Fiber-Reinforced High-Performance Concrete Based on Unit Cell Calculations. *Materials* **2024**, *17*, 2247. [CrossRef] [PubMed]

37. Pise, M.; Brands, D.; Schröder, J.; Gebuhr, G.; Anders, S. Macroscopic model for steel fiber reinforced high performance concrete based on unit cell calculations. *PAMM* **2021**, *21*, e202100180. [CrossRef]
38. *GB/T 50081-2019*; Standard for Test Method of Mechanical Properties on Ordinary Concrete. People's Republic of China National Standard; The State Bureau of Quality and Technical Supervision of the People's Republic of China: Beijing, China, 2003.
39. *GB50204-2015*; Construction Quality Acceptance Specification for Concrete Structure Engineering. People's Republic of China National Standard; China Building Industry Press: Beijing, China, 2015.
40. Guo, J.; Yu, H.; Ma, H.; Wu, Z. Damage and deterioration characteristics of basic magnesium sulfate cement-coral aggregate concrete exposed to elevated temperature. *Eng. Fail. Anal.* **2022**, *137*, 106275. [CrossRef]
41. *CECS 02-2005*; Technical Specification for Detecting Strength of Concrete by Ultrasonic-Rebound Combined Method. People's Republic of China National Standard; China Architecture & Building Press: Beijing, China, 2005.
42. Johnston, D.; Stokes, D.; Surdahl, R. A kinetic-based method for interpreting ASTM C 1260. *Cem. Concr. Aggreg.* **2000**, *22*, 142–149. [CrossRef]
43. Ruslan, I.; Farid, S.; Rashit, K.; Evgeny, K. The influence of a modeled aggressive medium upon the degradation of concrete structures: A physical and numerical model of research. *Buildings* **2024**, *14*, 1762. [CrossRef]
44. Fang, Q.; Zhang, J. Three-dimensional numerical modelling of concrete-like materials subjected to dynamic loadings. *Adv. Prot. Struct. Res.* **2012**, *1*, 33.
45. Wu, Z.; Zhang, J.; Yu, H.; Ma, H.; Chen, L.; Dong, W.; Huan, Y.; Zhang, Y. Coupling effect of strain rate and specimen size on the compressive properties of coral aggregate concrete: A 3D mesoscopic study. *Compos. Part B Eng.* **2020**, *200*, 108299. [CrossRef]
46. Holmquist, T.J.; Johnson, G.R. A computational constitutive model for glass subjected to large strains, high strain rates and high pressures. *J. Appl. Mech.* **2011**, *78*, 051003. [CrossRef]
47. Malvar, L.J.; Crawford, J.E.; Wesevich, J.W.; Simons, D. A plasticity concrete material model for DYNA3D. *Int. J. Impact Eng.* **1997**, *19*, 847–873. [CrossRef]
48. Wu, Z.; Zhang, J.; Yu, H.; Ma, H. 3D mesoscopic investigation of the specimen aspect-ratio effect on the compressive behavior of coral aggregate concrete. *Compos. Part B Eng.* **2020**, *198*, 108025. [CrossRef]
49. Diao, Y. *Research on Macroscopic Mechanical Properties of Concrete Interfacial Transition Zone and its Relationship with Microstructure*; Nanjing University of Aeronautics and Astronautics: Nanjing, China, 2021.
50. Kim, S.M.; Al-Rub, R.K.A. Meso-scale computational modeling of the plastic-damage response of cementitious composites. *Cem. Concr. Res.* **2011**, *41*, 339–358. [CrossRef]

Disclaimer/Publisher's Note: The statements, opinions and data contained in all publications are solely those of the individual author(s) and contributor(s) and not of MDPI and/or the editor(s). MDPI and/or the editor(s) disclaim responsibility for any injury to people or property resulting from any ideas, methods, instructions or products referred to in the content.